Journal of Magnetic Resonance 328 (2021) 106994

Contents lists available at ScienceDirect

Journal of Magnetic Resonance

journal homepage: www.elsevier.com/locate/jmr

On the use of single-frequency versus double-frequency satellite-transition pulses for MQMAS

Ivan Hung, Zhehong Gan *

National High Magnetic Field Laboratory, 1800 East Paul Dirac Drive, Tallahassee, FL 32310, USA

ARTICLE INFO

Article history:
Received 20 April 2021
Revised 28 April 2021
Accepted 29 April 2021
Available online 4 May 2021

Keywords:
Multiple quantum magic angle spinning
MQMAS
Triple quantum
Large quadrupolar interactions
Double-frequency
Cosine pulse
Satellite-transitions
Quadrupolar jolting frame
Double frequency
Cosine modulation
Average Hamiltonian
Spinning sidebands

ABSTRACT

It has been shown recently that a rotor-period long pulse applied at a frequency selective to the satellite-transitions of half-integer quadrupole nuclei can efficiently interconvert central-transition (CT) and triple-quantum (TQ) coherences for the acquisition of MQMAS spectra [I. Hung, Z. Gan, J. Magn. Reson. 324 (2021) 106913; doi: https://doi.org/10.1016/j.jmr.2021.106913]. By using a pair of such pulses and selecting opposite changes in coherence order, the anisotropic phase of the effective *rf* field can be refocused. Efficient multiple-quantum interconversion has led to low-power MQMAS pulse sequences capable of obtaining isotropic NMR spectra for the largest quadrupolar couplings to date. In this work, we extend the satellite-transition selective pulses from single- to double-frequency (or cosine) irradiation. By applying average Hamiltonian theory in the quadrupolar jolting frame, it is shown that the phase for TQ/CT conversion converges when the double-frequency irradiation matches the mirror-image symmetry of the satellite-transitions. The coherent conversion explains the mechanism behind the double-frequency sweep (DFS) and fast amplitude modulation (FAM) methods used for MQMAS. However, the strict matching condition limits the bandwidth of such double-frequency pulses to less than one spinning frequency. The use of a pair of identical cosine satellite-transition pulses is proposed to refocus the residual anisotropic phase spread. The refocusing leads to a more efficient MQMAS pulse sequence with a broader bandwidth suitable for large quadrupolar couplings and chemical shift ranges. Comparisons with the recently presented single-frequency lpMQMAS and other MQMAS pulse schemes show that cos-lpMQMAS is more efficient, less susceptible to fluctuations in spinning frequency, and suffers from less distortion in quadrupolar line shapes, as demonstrated with model compounds of moderate and large quadrupolar couplings, $^{87}RbNO_3$ and β-$^{71}Ga_2O_3$. In particular, the results for β-$^{71}Ga_2O_3$ show an order of magnitude increase in MQMAS efficiency.

1. Introduction

Since its introduction in 1995, multiple-quantum magic-angle spinning (MQMAS) [1] has become a widely used experiment for solid-state NMR of quadrupolar nuclei. The correlation under MAS of multiple-quantum (MQ) transitions with the central-transition (CT) of half-integer quadrupolar nuclei refocuses the second-order quadrupolar broadening, yielding high-resolution isotropic spectra. For disordered samples, the correlation allows separation and deconvolution of the chemical shift and the second-order quadrupolar shift distributions in two dimensions [2,3]. The efficiency of the MQMAS experiment, determined by the excitation and conversion of MQ coherences is of paramount importance to the application of MQMAS, especially for insensitive nuclei and samples. Its dependence on the quadrupolar couplings also affects line shapes and quantitative interpretation of MQMAS spectra. As described in a seminal paper published by Vega and Naor [4] before the introduction of MQMAS, MQ coherence can be excited and converted back to the CT through two mechanisms. The first is by applying an on-resonance *rf* pulse near the CT. Efficient excitation and conversion can be achieved when the quadrupolar splitting is close to the *rf* field strength. This mechanism requires short, strong *rf* pulses given that the typical quadrupole couplings are much larger than the *rf* field. The second method is by applying double-frequency irradiation away from the CT, matching the frequencies of the two satellite-transitions (STs). Selective inversion of the STs between the |±1/2 > and |±3/2 > spin states effectively interconverts the triple-quantum (TQ) and CT coherences necessary for a triple-quantum MQMAS experiment. Based on these two mechanisms, numerous pulse schemes, and NMR probes capable of delivering strong *rf* fields

* Corresponding author.
E-mail address: gan@magnet.fsu.edu (Z. Gan).

https://doi.org/10.1016/j.jmr.2021.106994
1090-7807/

have been developed to improve the MQMAS efficiency [5–11]. Nevertheless, the efficiency is still far from ideal despite these efforts, especially for samples with large quadrupolar couplings that far exceed practically achievable *rf* field strengths.

Recently, the authors have introduced the use of rotor-period-long (τ_r)-pulses selective to the STs for application in MQMAS [12], as well as for the satellite-transition magic-angle spinning (STMAS) experiment [13]. For τ_r-pulses under MAS, the *rf* frequency sweeps across the ST frequencies modulated by the sample rotation. The level crossings always occur regardless of how large the quadrupolar coupling is, as long as the applied *rf* frequency is within the span of the STs. The crossings can achieve transitions between the |±1/2> and |±3/2> spin states for STMAS and MQMAS. However, the timing of the level crossings varies among different crystallites in powder samples giving rise to an anisotropic phase spread in both TQ excitation and conversion that can cause signal cancellation. Inspired by the use of long pulses for ^{1}H-detected heteronuclear multiple-quantum correlation (HMQC) of quadrupole nuclei [14], MQMAS and STMAS pulse sequences were designed in a symmetric manner such that signal cancellation from the phase spread effect can be avoided. These long-pulse schemes, dubbed lpMQMAS and lpSTMAS due to their low-power requirement, can cover a wide range of quadrupole couplings and have been applied successfully to acquire MQMAS and STMAS spectra for the largest quadrupolar couplings to date [12,13].

In this work, we compare the use of ST-selective pulses with single- and double-frequency irradiation for MQMAS. By applying average Hamiltonian theory in the so-called quadrupolar jolting frame, we show that the phase for the TQ ↔ CT conversion diverges for single-frequency pulses causing signal loss, while for two-frequency irradiation the phase converges. The phase convergence explains why double-frequency irradiation in the form of double-frequency sweeps (DFSs) [6] and fast amplitude modulation (FAM) pulses [7,9] have been used successfully for MQMAS. However, it will be shown that the phase convergence occurs only for a narrow bandwidth, less than one MAS frequency. This narrow bandwidth can limit application of MQMAS to samples with large quadrupolar couplings and chemical shift ranges. Therefore, we propose the use of cosine (or double frequency) pulses in a pairwise manner to attain a broadband MQMAS experiment. In the following, we first present the average Hamiltonian theory used to derive the effective *rf* Hamiltonian in the quadrupolar jolting frame [14–16] for both single- and double-frequency long pulses. An analytical solution will be derived for a spin $S = 3/2$ system by assuming that the applied *rf* frequency is far off-resonance from the CT and selective only to the STs. The theoretical results show that a phase spread develops for TQ ↔ CT conversion when a single-frequency long pulse is applied, and the phase converges for double-frequency pulses. The phase spread can also be refocused by using identical long pulses for both the MQ excitation and conversion. Experimentally, the cosine low-power MQMAS method is compared with other MQMAS pulse schemes using the model compounds $^{87}RbNO_3$ with moderate quadrupolar couplings and β-$^{71}Ga_2O_3$ with large quadrupolar couplings.

2. Theory

In this section, we derive the spin dynamics of τ_r-pulses applied to $S = 3/2$ nuclei under MAS. The aim is not to provide a full general treatment, but rather to use a four-level system to understand the most salient features of 'long' pulse *rf* irradiation far off-resonance from the central-transition (CT). For such a case, it is possible to obtain an analytical solution for the *rf* spin dynamics, which elucidates an anisotropic effective *rf* field, in terms of both magnitude and phase. For larger spin quantum numbers, numerical simulations can be carried out to calculate the effects of the effective *rf* Hamiltonian under MAS.

Let us consider the Hamiltonian of a spin $S = 3/2$ nucleus under *rf* irradiation

$$H = H_Q + H_{rf}$$

$$H_Q(t) = q(t)[S_z^2 - S(S+1)/3] \tag{1}$$

$$H_{rf} = \omega_{1x}(t)S_x + \omega_{1y}(t)S_y$$

where the MAS-modulated first-order quadrupole coupling $q(t)$ is much larger than the magnitude of the *rf* field $|\omega_1|$. The *rf* Hamiltonian is expressed generally with the two components of the *rf* field vector in the transverse plane $\omega_1 = \omega_{1x} + i\omega_{1y}$. The offset terms from the chemical shift and second-order quadrupolar coupling are not considered here, but will be briefly discussed later.

As a first step to simplifying the Hamiltonian, we go to the interaction representation of the quadrupolar interaction $H_Q(t)$, also known as a jolting frame [15], described by the rotation operator R,

$$\begin{aligned} R &= \exp\left[-i\int_0^t H_Q(t')dt'\right] \\ h_{rf}(t) &= R(t)H_{rf}R(t)^{-1} \end{aligned} \tag{2}$$

The jolting frame moniker is used to describe this time-dependent rotation to distinguish it from the well-known NMR rotating frame that precesses at a constant Larmor frequency. In the quadrupolar jolting frame (QJF), the leading $H_Q(t)$ term is eliminated along with the frequency offset from the large first-order quadrupolar coupling, but additional MAS modulations are introduced into the *rf* Hamiltonian

$$h_{rf}(t) = \frac{\sqrt{3}}{2}\begin{vmatrix} 0 & \omega_1(t)e^{i\varphi_Q(t)} & & \\ \omega_1^*(t)e^{i\varphi_Q(t)} & 0 & \blacksquare & \\ & \blacksquare & 0 & \omega_1(t)e^{-i\varphi_Q(t)} \\ & & \omega_1^*(t)e^{-i\varphi_Q(t)} & 0 \end{vmatrix} \tag{3}$$

where $\varphi_Q(t) = 2\int_0^t q(t')dt'$ is the rotation phase of the jolting frame. In Eq. (3), we assume that the *rf* irradiation is applied far off-resonance from the CT such that the CT elements of the *rf* Hamiltonian (denoted by black squares) can be neglected. This allows the *rf* Hamiltonian to be separable into two independent two-level subspaces corresponding to the two satellite-transitions (STs). The QJF introduces $e^{i\varphi_Q(t)}$ and $e^{-i\varphi_Q(t)}$ modulations that are related to the spinning sideband (ssb) intensities s_k for the ST MAS spectra, as obtained by Fourier expansion

$$\begin{aligned} e^{i\varphi_Q(t)} &= \textstyle\sum_k s_k e^{ik\omega_r t} \\ e^{-i\varphi_Q(t)} &= \textstyle\sum_k s_{-k}^* e^{ik\omega_r t} \end{aligned} \tag{4}$$

Thus, insights into the behavior of the *rf* Hamiltonian in Eq. (3) can be gained by examining the ST ssbs. To illustrate, simulated ssbs for the two STs of a single $S = 3/2$ crystallite are shown in Fig. 1b. The ssb manifolds span the static ST powder patterns (Fig. 1a), which have a breadth of approximately $1.5\nu_Q$, where $\nu_Q = 3C_Q/[2S(2S-1)]$ is the quadrupole coupling frequency. The phase and magnitude of the ssbs vary widely even for the same crystallite when the rotor phase γ changes. Taking the normalization condition $\sum s_k^2 = 1$, the mean magnitude of the s_k values can be estimated from the number of ssbs within the span of ~$1.5\nu_Q$,

$$\langle|s_k|\rangle \sim \sqrt{\nu_r/1.5\nu_Q} < 1 \tag{5}$$

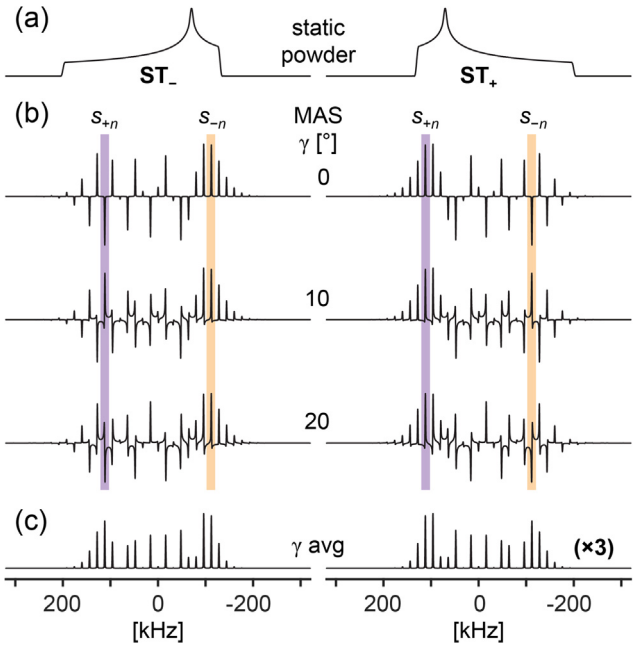

Fig. 1. Numerical spectral simulations for the two satellite-transitions of a $S = 3/2$ spin: (a) static powder pattern, and MAS spinning sidebands of an individual crystallite with (b) small differences in rotor angle/phase γ, and (c) powder averaged over γ. The simulations illustrate that both the magnitude and phase of spinning sidebands vary widely among crystallites in a powder sample, especially noting that the effective *rf* Hamiltonian of τ_r-pulses is scaled by the complex intensity of the spinning sideband being irradiated. The s_{+n} and s_{-n} ssbs highlighted with purple and orange vertical bars represent *rf* pulse irradiation at $+n\omega_r$ and $-n\omega_r$, respectively. Parameters used for SIMPSON [17] simulations: $C_Q = 2\nu_Q = 400$ kHz, $\eta_Q = 0.3$, $\alpha = 0$, $\beta = 30°$ and $\omega_r/2\pi = 16$ kHz. (For interpretation of the references to color in this figure legend, the reader is referred to the web version of this article.)

It should be emphasized that there is a large difference between the ssb intensities of an individual crystallite s_k (Fig. 1b) and the absorptive sideband intensities s_k^2 that are observed experimentally for powder samples after averaging over the rotor-angle γ (Fig. 1c). Furthermore, the two STs have mirror image symmetry, i.e., the ssbs of one ST (e.g., s_k) are complex conjugates of the other ST with the opposite sideband order (e.g., s^*_{-k}).

In the QJF, the *rf* Hamiltonian has many oscillating components modulated by the sideband intensities s_k. Average Hamiltonian theory or Floquet theory can be invoked to derive an effective *rf* Hamiltonian for the spin dynamics of τ_r-pulses. Without losing generality, we consider *rf* irradiation at a frequency $-n\omega_r$ away from the CT such that the *rf* Hamiltonian is cyclic with the rotor period $\tau_r = 2\pi/\omega_r$ in the QJF. Average Hamiltonian theory can be applied by simply taking the constant s_n and s_{-n} terms from Eqs. (3) and (4),

$$\bar{h}_{rf} = \pi\nu_1\sqrt{3}\begin{vmatrix} 0 & s_n & & \\ s_n^* & 0 & & \\ & & 0 & s_{-n} \\ & & s_{-n}^* & 0 \end{vmatrix} \tag{6}$$

This Hamiltonian and its evolution operator can be expressed in fictious spin-1/2 operators (I_x, I_y, I_z) for the two STs denoted by ±,

$$\bar{h}_{\pm} = 2\pi\nu_1\sqrt{3}|s_{\pm n}|\exp(\mp i\varphi_{\pm n}I_z)I_x\exp(\pm i\varphi_{\pm n}I_z) \tag{7}$$

$$U(t) = \begin{vmatrix} \exp\left(-i\bar{h}_+t\right) & 0 \\ 0 & \exp\left(-i\bar{h}_-t\right) \end{vmatrix} \tag{8}$$

From Eq. (7), it can be seen that the effective *rf* Hamiltonians $\bar{h}_{\pm}$ for the two STs are scaled by the magnitude $|s_{\pm n}|$ and phase-shifted by $\varphi_{\pm n}$, the phase of the ssb at the frequency irradiated by the τ_r-pulse. As illustrated by the simulations in Fig. 1, the spinning sidebands $s_{\pm n}$ vary widely with crystallite orientation, therefore the *effective rf field is anisotropic in both amplitude and phase.*

The evolution of the full density operator

$$\sigma = \begin{vmatrix} p_{+3/2} & \mathrm{ST}_+ & \mathrm{DQ}_+ & \mathrm{TQ} \\ \mathrm{ST}_+^* & p_{+1/2} & \mathrm{CT} & \mathrm{DQ}_- \\ \mathrm{DQ}_+^* & \mathrm{CT}^* & p_{-1/2} & \mathrm{ST}_- \\ \mathrm{TQ}^* & \mathrm{DQ}_-^* & \mathrm{ST}_-^* & p_{-3/2} \end{vmatrix} \tag{9}$$

can be separated into blocks for the two ST subspaces. The CT and TQ coherences are in the antidiagonal block σ_M together with the double-quantum ST coherences DQ_+ and DQ_-

$$\sigma_M = \begin{vmatrix} \mathrm{DQ}_+ & \mathrm{TQ} \\ \mathrm{CT} & \mathrm{DQ}_- \end{vmatrix} \tag{10}$$

Their evolution can be obtained explicitly by multiplying out $U(t)\sigma U(t)^{-1}$ from Eqs. (8) and (10),

$$\sigma_M(t) = e^{-i\bar{h}_+t}\sigma_M(0)e^{i\bar{h}_-t} \tag{11}$$

It is important to note that the evolution of σ_M is sandwiched by the effective Hamiltonians $\bar{h}_+$ and $\bar{h}_-$ of the two different STs. By setting the initial conditions to $\sigma_M(0) = \begin{vmatrix} 0 & 0 \\ 1 & 0 \end{vmatrix}$ for CT coherence, and $\sigma_M(0) = \begin{vmatrix} 0 & 1 \\ 0 & 0 \end{vmatrix}$ for TQ coherence, one can obtain the efficiency for MQ excitation (f_{exc}) and conversion (f_{conv})

$$\begin{aligned} f_{\mathrm{exc}} &= \sin\tfrac{\theta_+}{2}\sin\tfrac{\theta_-}{2}\exp\left[-i(\varphi_{+n}+\varphi_{-n})\right] \\ f_{\mathrm{conv}} &= \sin\tfrac{\theta_+}{2}\sin\tfrac{\theta_-}{2}\exp\left[i(\varphi_{+n}+\varphi_{-n})\right] \end{aligned} \tag{12}$$

using the spin-1/2 rotation operator ([18], Eq. 3.2.45),

$$\exp\left(\mp i\bar{h}_{\pm}t\right) = \begin{vmatrix} \cos\frac{\theta_{\pm}}{2} & \mp i\exp(-i\varphi_{\pm n})\sin\frac{\theta_{\pm}}{2} \\ \mp i\exp(i\varphi_{\pm n})\sin\frac{\theta_{\pm}}{2} & \cos\frac{\theta_{\pm}}{2} \end{vmatrix} \tag{13}$$

where $\theta_{\pm} = 2\pi\nu_1\sqrt{3}|s_{\pm n}|t$ are the nutation angles of the effective *rf* field for the two STs. Eq. (12) shows phase factors $\exp[\mp i(\varphi_{+n} + \varphi_{-n})]$ that have opposite signs for MQ excitation and conversion, and are equal to the sum of the phase of the effective *rf* fields for the two STs. Considering that the effective *rf* field is scaled by the $+n$th and $-n$th ssbs of the STs irradiated by long pulses, we can use the amplitudes and phases of the ssbs in Fig. 1b to visualize the MQ excitation and conversion behavior for powder samples. The $+n$th and $-n$th order ssbs of one ST show no inherent correlation with each other, so a powder average or even just a γ-average leads to signal cancellation due to the phase differences between different crystallites, as evidenced by the significantly lower magnitude after γ-averaging (Fig. 1c). When a single τ_r-pulse is applied for CT ↔ TQ interconversion at $-n\omega_r$, the lack of any correlation between the s_{-n} ssbs of the two STs (or equivalently, between the s_{+n} and s_{-n} ssbs of one of the STs), results in largely incoherent signals which would cancel each other from the powder average. However, when a pair of identical rotor-synchronized τ_r-pulses are used, the opposite signs in the phase factors of f_{exc} and f_{conv} cancel each other, or are 'refocused', leading to an overall MQMAS efficiency without signal cancellation from the anisotropic phase

$$f_{\mathrm{lpMQMAS}} = \langle f_{\mathrm{exc}} \cdot f_{\mathrm{conv}}\rangle = \langle \sin^2\frac{\theta_+}{2}\sin^2\frac{\theta_-}{2}\rangle \tag{14}$$

where $\langle\ \rangle$ denotes a powder average.

Ideally, full inversions of the STs with $\theta_{\pm} = \pi$ pulses would give complete TQ ↔ CT interconversion. For powder samples, this condition cannot be met given the wide distribution in the magnitude of effective *rf* fields caused by the large variation in ssb intensities in Fig. 1b. Using the mean ST ssb intensity $|s_k| \sim \sqrt{\nu_r/1.5\nu_Q}$ from Eq. (5), we can estimate the optimal *rf* field for ST inversion using a τ_r-pulse to be

$$\nu_1^{opt} = \sqrt{\nu_r \nu_Q/6} \tag{15}$$

The theory up to this point describes the essence of the previously reported low-power MQMAS (lpMQMAS) experiments [12], which use a pair of single-frequency τ_r-pulses.

The cancellation of the anisotropic phases in f_{exc} and f_{conv} requires rotor-synchronization of the two τ_r-pulses. The simulations in Fig. 1b show that the phase of individual sidebands s_n for the effective *rf* field are very sensitive to the rotor angle γ. Spinning instability can affect the timing between the two pulses, and consequently introduce incomplete phase cancellation resulting in signal decay and t_1-noise. This timing error is proportional to the t_1-evolution time, thus it can problematic for samples with narrow isotropic peaks. These adverse effects were observed after the publication of the previous lpMQMAS work [12] and have motivated the investigation of using double-frequency cosine τ_r-pulses, as inspired by previous work on double-frequency sweep (DFS) [6] and fast amplitude modulation (FAM) [7,9] methods for MQMAS.

Under cosine irradiation, two *rf* components irradiate the STs symmetrically on both sides of the CT simultaneously. The first-order average Hamiltonian is additive, therefore the effective *rf* Hamiltonian of cosine pulse is simply a sum of the s_n and s_{-n} terms from the two *rf* components in Eq. (6),

$$\bar{h}_{rf}^{cos} = \frac{\sqrt{3}}{2}\pi\nu_1 \begin{vmatrix} 0 & s_n + s_{-n} & & \\ (s_n + s_{-n})^* & 0 & & \\ & & 0 & (s_n + s_{-n})^* \\ & & s_n + s_{-n} & 0 \end{vmatrix} \tag{16}$$

We can continue deriving the efficiency for MQ excitation and conversion following the same procedure in Eqs. (11)-(13). Everything is the same except that the effective Hamiltonian for the two STs $\bar{h}_+$ and $\bar{h}_-$, are now complex conjugates of each other, as evident from Eq. (16). This is the key for the double-frequency cosine pulses which make the phase factor for CT ↔ TQ interconversion in Eq. (12) disappear. In addition, the amplitudes of the effective *rf* fields become the same for the two STs

$$f_{exc}^{cos} = f_{conv}^{cos} = \sin^2\frac{\bar{\theta}}{2} \tag{17}$$

where $\bar{\theta} = \pi\nu_1\sqrt{3}|s_{+n} + s_{-n}|t$ is the nutation angle of the effective *rf* field for cosine pulses. Eq. (17) explains why cosine amplitude modulated, DFS or FAM pulses can be used for TQ → CT conversion in MQMAS without the issues of anisotropic phase and signal cancellation, in contrast to a single-frequency τ_r-pulse. This phase coherent feature has previously been observed for FAM pulses shorter than one rotor period via numerical simulations [19].

The complex conjugate relationship between $\bar{h}_+$ and $\bar{h}_-$ for double-frequency cosine pulses arises from the mirror image symmetry of the STs. The cosine pulse must be centered at the center band position of the STs such that irradiation occurs for the same s_n and s_{-n} ssbs of the two STs. When the two irradiation frequencies deviate from this strict symmetry requirement, for instance, due to chemical shift dispersion and/or the second-order quadrupolar shift, the complex conjugate relationship is broken giving rise to residual anisotropic phase and signal loss if not refocused. Examination of Fig. 1b shows that there is no apparent correlation between adjacent ST ssbs, thus, one can expect the bandwidth due to the anisotropic phase to be less than one spinning frequency ν_r. This bandwidth problem can be avoided by using a pair of identical cosine τ_r-pulses to refocus the residual anisotropic phase. Since the residual anisotropic phase of double-frequency irradiation should inherently be smaller than that of single-frequency τ_r-pulses, the timing requirement for two identical cosine τ_r-pulses should be less stringent compared to single-frequency τ_r-pulses.

The main contributing factor to the efficiency of lpMQMAS is the distribution of the effective pulse nutation angles $\theta_{\pm}$ in Eq. (12). In comparison with the efficiency of the single-frequency case in Eq. (14), the overall efficiency for double-frequency cos-lpMQMAS is given by

$$f_{lpMQMAS}^{cos} = \langle \sin^4\frac{\bar{\theta}}{2} \rangle \tag{18}$$

For the optimal *rf* field, we can compare the scaling factors between the single- and double-frequency cases, $\langle s_n \rangle$ and $\langle s_n + s_{-n} \rangle/2$. Assuming a completely random phase distribution for the complex ssb intensities $\langle s_n \rangle$, a statistical average would make the latter term $\langle s_n + s_{-n} \rangle/2$ smaller by a factor of $\sqrt{2}$. Thus, the optimum ν_1 for cos-lpMQMAS is correspondingly larger by $\sqrt{2}$ compared to Eq. (15),

$$\nu_1^{opt} = \sqrt{\nu_r \nu_Q/3} \tag{19}$$

Interestingly, this result agrees with the assumption of equal power density between single- and double-frequency irradiation.

For comparison between the powder averaged MQMAS efficiencies for single- and double-frequency pulses, we can express Eqs. (14) and (18) in different forms

$$\begin{aligned} f_{lpMQMAS} &= \{1 - \langle \cos\theta_+ + \cos\theta_- \rangle + \langle \cos\theta_+ \cos\theta_- \rangle\}/4 \\ f_{lpMQMAS}^{cos} &= \left\{1 - 2\langle \cos\bar{\theta} \rangle + \langle \cos^2\bar{\theta} \rangle\right\}/4 \end{aligned} \tag{20}$$

The second terms are similar between the two when the *rf* field is optimized. However, the third term always favors the double-frequency case because there is no cancellation of the square term $\langle \cos^2\bar{\theta} \rangle$, contributing to a higher efficiency. The higher efficiency along with the refocused anisotropic phase, broad bandwidth, and relaxed rotor synchronization requirement highlight the benefits of using a pair of cosine τ_r-pulses for MQMAS pulse sequences.

The theory presented so far has neglected the offsets from the second-order quadrupolar coupling and chemical shift by assuming that the effective *rf* nutation is on-resonance with the spinning sidebands being irradiated. This assumption has simplified the analytical results for MQ excitation and conversion obtained using average Hamiltonian theory. Small offsets can be treated by a nutation about a tilted effective *rf* field off the transverse plane. This offset should always be less than half of the spinning frequency otherwise a jolting frame closer to the neighboring spinning sideband would be chosen. A more general treatment of this problem can be carried out using Floquet theory. For simplicity, average Hamiltonian theory was used here to describe the mechanism of single- and double-frequency ST-selective pulses for MQMAS experiments.

3. Results and discussions

Fig. 2 shows MQMAS pulse sequences and their corresponding spectra for a $S = 3/2$ model compound, $^{87}RbNO_3$. The compound has three ^{87}Rb sites with moderate quadrupolar couplings ($C_Q \sim 2$-MHz) [20]. Comparisons among the MQMAS methods were carried out using various combinations of MQ excitation and conversion elements. Phase-modulated whole-echo signals were acquired with a 96-step phase cycle that selects the coherence transfer

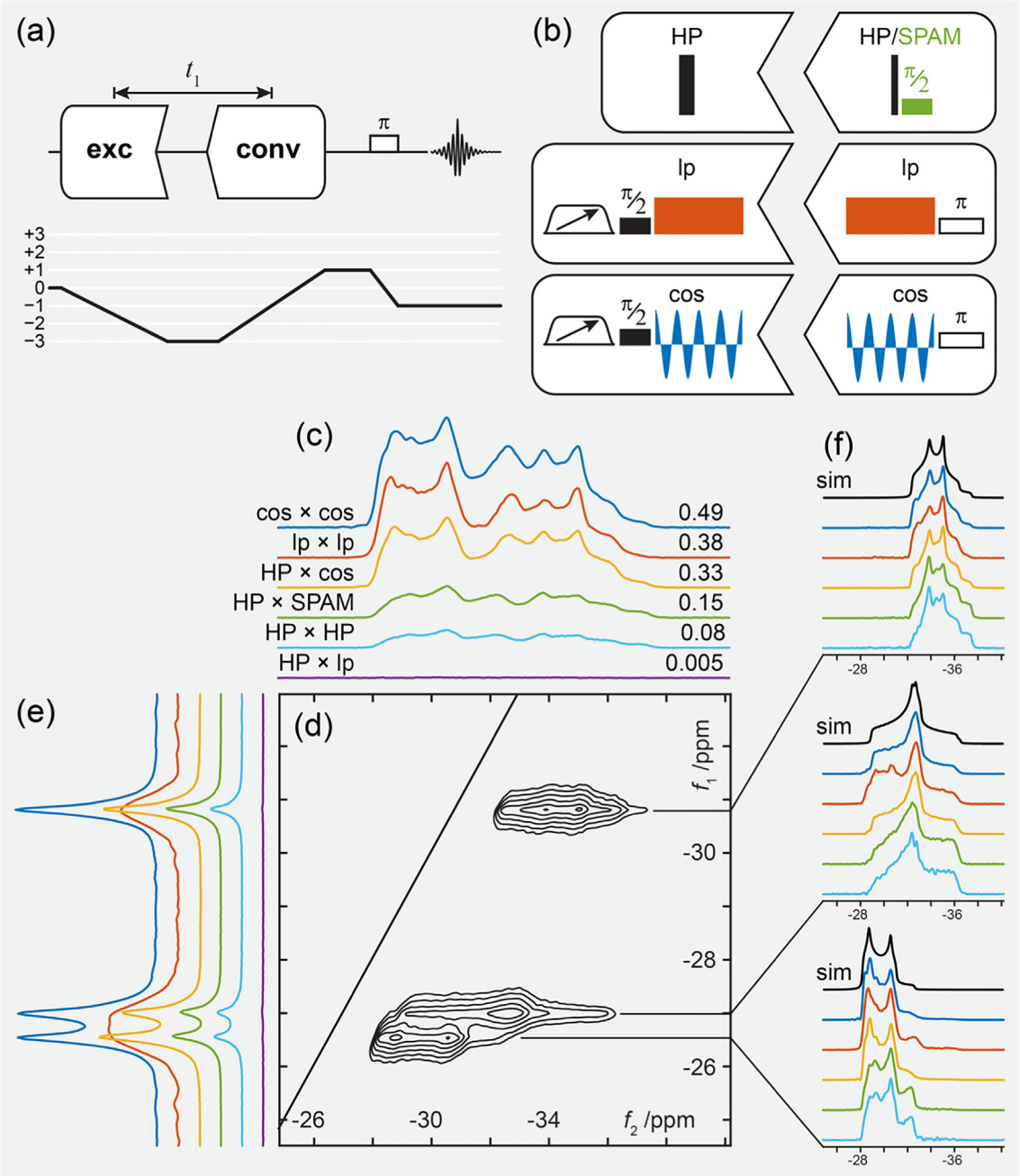

Fig. 2. (a) MQMAS shifted-echo pulse sequence with coherence transfer pathway diagram, (b) 3Q excitation and conversion elements used in this work, (c) 1D ^{87}Rb MQMAS spectra of $RbNO_3$ acquired with $t_1 = \tau_r$ shown in magnitude mode, and (d) 2D ^{87}Rb shifted-echo cos-lpMQMAS spectrum of $RbNO_3$ along with (e) f_1 and (f) f_2 sum projections using different combinations of the elements in (b). All spectra were acquired at 14.1 T with a Bruker Avance NEO console, ν_r = 10 kHz MAS, recycle delay of 0.4 s, CT-selective π/2- and π-pulses of 20 and 40 μs at ν_1 = 6.25 kHz, and full-echo acquisition with a half-echo delay of 10 ms. MQMAS parameters: 3Q hard-pulse (HP) excitation and conversion pulses of 6.6 and 2.85 μs with ν_1 = 86.7 kHz; soft-pulse-added-mixing (SPAM) pulse of 20 μs at ν_1 = 6.25 kHz. All τ_r-pulses had a duration of $1/\nu_r$ = 100 μs, single-frequency low-power (lp) pulses were applied with ν_1 = 36.4 kHz at an offset of +270 kHz, while cos τ_r-pulses used ν_1 = 48.5 kHz and an amplitude modulation frequency of 170 kHz, as optimized experimentally. Signal enhancement was applied for lpMQMAS in all instances using a 1 ms WURST-80 pulse with a sweep range equal to ν_r, ν_1 = 16.2 kHz, and a transmitter offset of + 270 kHz. The 2D shifted-echo MQMAS spectra was acquired with 128 rotor-synchronized t_1 increments, and 96 transients per increment, resulting in a total experiment time of 82 min.

pathway depicted in Fig. 2a. For all efficiency comparisons, an effective $t_1 = \tau_r$ increment was used with the duration between the centers of the excitation and conversion pulses matching one rotor period, and by measuring the total integrated intensity of the magnitude spectra relative to that of a spin-echo spectrum.

The efficiency comparisons in Fig. 2c start from the original MQMAS sequence using hard pulses for MQ excitation and conversion (HP × HP) [1,21]. An 8% efficiency was obtained after pulse length optimization using an *rf* field of ν_1 = 86.7 kHz. The efficiency is low because the *rf* field is relative weak compared to the magnitude of the ^{87}Rb quadrupolar couplings in $RbNO_3$. Inclusion of a so-called soft-pulse-added-mixing (SPAM) [22] pulse (HP × SPAM) increases the efficiency to 15%. The second hard pulse converts TQ coherence to p = +1, 0, −1 CT coherences simultaneously, and constructive addition of these three contributions using a CT-selective π/2-pulse increases the conversion efficiency [22]. The

use of a cosine τ_r-pulse (HP × cos) is far more efficient than either hard pulse conversion scheme, more than doubling the efficiency to 33%. Cosine amplitude modulation of the pulse is equivalent to splitting the *rf* field into two components that selectively irradiate the two STs simultaneously. This is similar to the case of the commonly used FAM and DFS methods [6,7,9]. A Fourier expansion of the square modulated FAM sequence becomes equivalent to the main cosine components plus other smaller high-frequency harmonics [19]. We have compared and found similar performance between pure cosine and FAM square modulations, as would be expected. For DFS, we observed no extra enhancement after adding a frequency sweep to the cosine τ_r-pulse (results not shown). In order to reduce the number of parameters for optimization, comparisons presented here are limited to single-frequency and cosine double-frequency pulses.

Making the MQ excitation and conversion pulses selective to STs restricts the coherence transfer for the desired MQMAS pathway from spreading to other transitions. This is the main mechanism for enhanced TQ → CT conversion for the cosine, FAM and DFS schemes. However, Fig. 2c shows a very different result when using just one single-frequency satellite-selective low-power (lp) pulse (HP × lp), which gives almost no signal (<0.5%). This is the consequence of the anisotropic phase of the effective *rf* field, which cancels the signal when not refocused. This cancellation does not occur for double-frequency irradiation as the phase for the MQ conversion converges as shown by theory in Eq. (17).

Better performances were obtained by using a pair of identical ST-selective τ_r-pulses. The most pronounced change is for (HP × lp) compared to (lp × lp), going from <0.5% to 38%! (Fig. 2c). This dramatic change illustrates how the anisotropic phase from a single τ_r-pulse is refocused by another τ_r-pulse to avoid signal cancellation, and why their application is possible in lpMQMAS experiments, as previously reported [12]. The highest efficiency (49%) is obtained using two cosine τ_r-pulses (cos × cos), a ~30% increase over two single-frequency lp τ_r-pulses (lp × lp). This enhancement confirms the result obtained in Eq. (20) from the powder statistical average of the τ_r-pulse nutation angles since the nutation angles for the two STs are the same for cosine pulses but different for single-frequency pulses.

Fig. 2d shows an isotropic-sheared 2D ^{87}Rb MQMAS spectrum that resolves the three crystalline sites in $RbNO_3$. The f_1 projections (Fig. 2e) show similar resolution among all MQMAS pulse schemes except the one using two single-frequency lp pulses (lp × lp). For the single-frequency case, precise rotor-synchronization between the excitation and conversion pulses is required to cancel the anisotropic phase in Eq. (12). Small deviations affect the refocusing of the anisotropic phase and consequently attenuate the time-domain signal intensity. The amount of mis-synchronization is proportional to the number of rotor cycles in the t_1 period, therefore its effect is more evident for MQMAS spectra of samples with narrow isotropic line widths. Given that the signal attenuation increases with t_1, the spinning speed fluctuations contribute to additional line broadening in the f_1 dimension and also generate t_1-noise. In contrast, the isotropic spectrum acquired using two cosine pulses (cos × cos) shows no such adverse effects. The converged MQ excitation and conversion for cosine pulses without a phase factor, Eq. (17) as compared to Eq. (12), makes the experiment much less sensitive to rotor synchronization between the two τ_r-pulses.

The f_1 isotropic projections in Fig. 2e also show how the spectral quantitation and line shapes vary among the different MQMAS pulse sequences due to their dependence on the magnitude of the quadrupolar couplings C_Q. There are small differences in C_Q among the three ^{87}Rb sites in $RbNO_3$ (C_Q[MHz] = 1.7, 2.0, 1.8). The middle peak has the largest quadrupolar coupling as judged from the width of its second-order quadrupolar pattern. The integrated sum projections in Fig. 2e show that the middle peak has a lower intensity than the other two sites when at least one hard pulse is used for MQ excitation and/or conversion since such pulses are known to be sensitive to the size of C_Q [23]. For lp and cos τ_r-pulses, Eqs. (15) and (19) show that their optimal *rf* fields are proportional to $\sqrt{\nu_r \nu_Q}$, making them much less sensitive to variations in C_Q magnitude. In particular, the (cos × cos) f_1 spectrum shows nearly identical peak heights among all three sites in $RbNO_3$, in agreement with the 1:1:1 ratio among the distinct crystallographic sites. Dependence of the MQMAS efficiency on C_Q also affects the quadrupolar line shapes obtained along the f_2 dimension of 2D MQMAS spectra. The comparison of f_2 slices in Fig. 2f for the three sites in $RbNO_3$ clearly shows less line shape distortions for spectra acquired using τ_r-pulses compared to short hard pulses.

The results above show the importance of refocusing the anisotropic phase in MQMAS experiments. For cosine pulses, the phase of MQ excitation or conversion converges because the two irradiation frequencies match the mirror image symmetry of the two satellite-transitions, i.e., when the same s_{+n} and s_{-n} ssbs are irradiated for the two STs. All MQMAS spectra in Fig. 2 were acquired using a carrier frequency near the CT signals of $RbNO_3$. For samples with larger quadrupolar couplings and chemical shift ranges, mirror image irradiation of the STs may not occur for all sites. To investigate such a scenario, a frequency offset ν_{off} was added to the cosine τ_r-pulses for the (HP × cos) and (cos × cos) MQMAS sequences presented above. Indeed, the frequency profile in Fig. 3c shows a bandwidth narrower than the MAS frequency when a single cosine pulse is used. As mentioned in the Theory section,

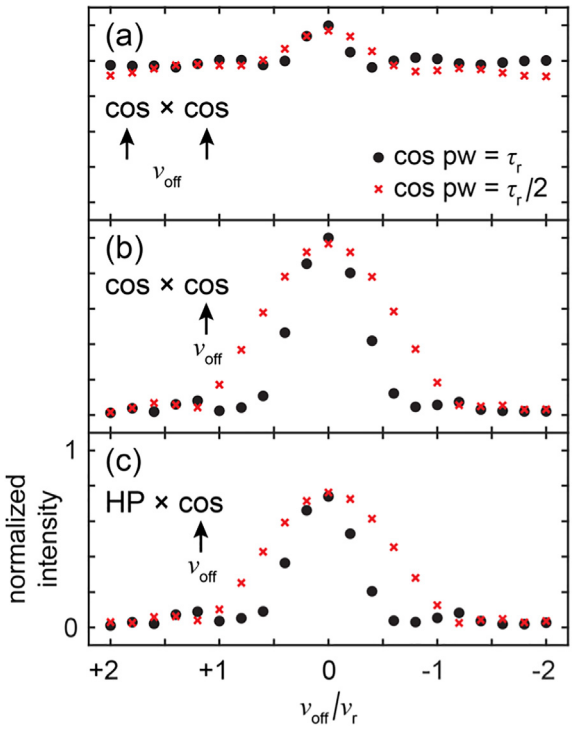

Fig. 3. Frequency profiles for MQMAS using cosine pulses one (black filled circles) and half (red crosses) rotor periods long. The frequency profiles were measured from the integrated intensity of the three Rb sites of $RbNO_3$ as a function of the frequency offset ν_{off} added onto the cosine pulses that are marked by arrows. In all cases, the cosine amplitude modulation frequency was kept at 170 kHz. The frequency offset for all other pulses including the unshifted cosine pulse in (b) were fixed to the CT position ν_{off} = 0 kHz. All other experimental parameters were the same as in Fig. 2 except the *rf* field for the τ_r/2 cosine pulses was optimized to ν_1 = 61.3 kHz compensating for the shorter pulse length. (For interpretation of the references to color in this figure legend, the reader is referred to the web version of this article.)

the phase for MQ excitation or conversion converges because of the complex conjugate (or mirror image) relationship between the two STs which gets carried into the effective *rf* field as described in the QJF. When a frequency offset is added to cosine pulses, the two irradiation frequencies begin to deviate from this conjugate condition. Thus, signal cancellation due to anisotropic phase is reintroduced, similar to the case of using just one single-frequency τ_r-pulse. The narrow bandwidth can be avoided by using two identical cosine τ_r-pulses because the anisotropic phase arising from MQ excitation gets canceled/refocused by that from MQ conversion, similar to the case of single-frequency τ_r-pulses discussed in Eqs. (12) and (14). The refocusing leads to a flattened frequency profile as shown in Fig. 3a. It is important to note that the two cosine pulses must be identical, including the added frequency offsets. Otherwise, the bandwidth remains narrow, as for the case of (HP × cos), when one of the cosine pulses is offset with respect to the other (Fig. 3b).

Besides the broadened frequency profiles, Fig. 3a also shows a small bump in efficiency centered at ν_{off} = 0 kHz for the (cos × cos) scheme. This elevated efficiency shares the same origin as the phase convergence and additional enhancement, 49% vs. 38%, over the (lp × lp) scheme observed in Fig. 2. Under double-frequency irradiation the effective *rf* Hamiltonians are complex conjugates of each other for the two ST subspaces, leading to equal nutation angles for the two STs. As a result, Eq. (20) shows a statistically higher overall MQMAS efficiency for cosine pulses than for single-frequency pulses from the statistical powder averaging of the effective *rf* amplitude. This additional efficiency becomes lost when an offset is added to the cosine pulses, as the complex conjugate relationship mentioned above no longer holds. The experimentally observed enhancement for the (cos × cos) scheme compared to (lp × lp) in Fig. 2c agrees with the bump in amplitude around ν_{off} = 0 kHz (Fig. 3a).

Strictly speaking, the use of cosine pulses for MQMAS is not original. The same mechanism has been employed for the DFS and FAM schemes, which selectively invert the STs to convert TQ into CT coherence for MQMAS. The main differences of the implementations in the current work are in the pulse durations and, most importantly, pairwise application to refocus the anisotropic phase of the effective *rf* field. Long pulses benefit from level-crossings between the *rf* field and the ST frequencies, overcoming large frequency offsets. It has been shown that the full benefit begins when pulses are at least $\tau_r/3$ in duration where most spins in powder samples experience one level-crossing. A strong *rf* field is needed to make the passage adiabatic and invert the STs. For longer pulses, STs experience multiple crossings and the effect from passages accumulate, lowering the *rf* field requirement. Frequency profiles for cosine pulses of duration $\tau_r/2$ (red crosses) are also shown in Fig. 3. As expected, the bandwidth is twice that of a τ_r-pulse when a single cosine pulse is used (Fig. 3c) but remains relatively similar when two identical cosine pulses are used (Fig. 3a). In this instance, the optimal *rf* field is found to be a factor of ~1.26 lower for the τ_r-pulses than for the $\tau_r/2$-pulses. In principle the optimal *rf* field can be lowered further by using longer pulses, however, acquisition of the $t_1 = \tau_r$ increment would be prevented due to the longer pulse durations. Taking this into consideration, τ_r-pulses are recommended, reducing the parameters for optimization and allowing acquisition of 2D MQMAS spectra with rotor-synchronized t_1 evolution starting from $t_1 = \tau_r$. The missing t_1 = 0 point can be compensated by a right-shift in the time-domain signal, or equivalently, by a 360° first-order spectral phase correction, followed by a shift of the spectral baseline during data processing. In case of spectral folding due to large 3Q chemical shifts, the *Q*-shear method can be applied to unfold spectra [24].

The use of cosine double-frequency τ_r-pulses in MQMAS for much larger quadrupolar couplings is demonstrated with β-Ga_2O_3 which has two inequivalent ^{71}Ga sites (S = 3/2, $\nu_Q(Ga^{VI})$ = 4.15 and $\nu_Q(Ga^{IV})$ = 5.6 MHz.) [25]. A number of overlapping CT ssbs are present in the 1D MAS spectrum due to the large second-order quadrupolar couplings. In addition, there is a large difference in chemical shift between the two sites. A high MQMAS efficiency and broad bandwidth are critical for acquisition of MQMAS spectra of such systems. Fig. 4 shows almost no signal for the (HP × cos) MQMAS pulse scheme, with ~3% efficiency for the small C_Q site. The efficiency enhancement from using a pair of τ_r-pulses is dramatic, nearing an order of magnitude. The (cos × cos) scheme performs better than the previously reported single-frequency (lp × lp) scheme [12] in three aspects. First, the efficiency is about 30% higher. Second, there is a smaller difference in efficiency between the two ^{71}Ga sites, which have a relatively large difference in C_Qs. Third, the isotropic f_1 projections show narrower line widths and less t_1-noise. All three observations agree with results obtained for the model sample with moderate quadrupolar couplings, $^{87}RbNO_3$.

We have chosen two model compounds of S = 3/2 nuclei to demonstrate the cos-lpMQMAS pulse sequence. The evolution of the two-level ST systems can be solved analytically to show the mechanism of ST-selective τ_r-pulses for the TQ ↔ CT transfer of MQMAS. The *rf* action by a τ_r-pulse is confined within the two-level ST system making the desired coherence transfer highly efficient. For S > 3/2 spins, the mechanism of level-crossing is still applicable for covering large quadrupolar couplings. However, the desired TQ ↔ CT transfer becomes less confined as compared to the two-level STs of S = 3/2 nuclei resulting in relatively lower efficiencies for S > 3/2 nuclei. Nevertheless, the leakage transfers, for example 5Q ↔ CT, offer opportunities for acquiring MQMAS spectra of higher quanta which have characteristics different from 3QMAS.

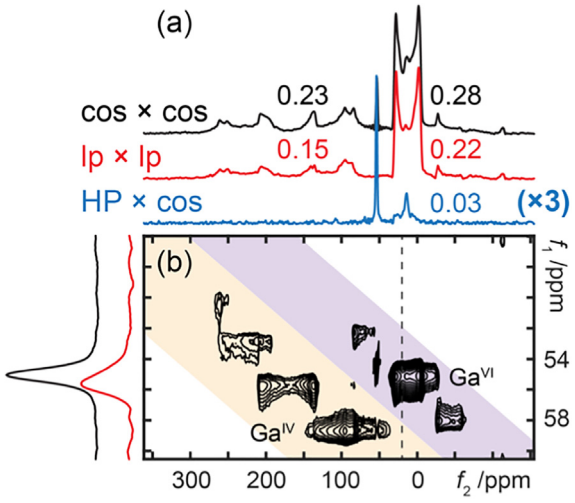

Fig. 4. (a) 1D ^{71}Ga (S = 3/2) MQMAS spectra of β-Ga_2O_3 acquired with $t_1 = \tau_r$ shown in magnitude mode with efficiency values compared to a spin-echo spectrum. (b) 2D ^{71}Ga cos-lpMQMAS spectrum of β-Ga_2O_3 along with f_1 slices for the center band of the Ga^{VI} site as marked by the vertical dashed line. The 2D spectrum is sheared into an isotropic f_1 representation and there is spectral aliasing due to the small f_1 spectral window from rotor-synchronized t_1 evolution. All MQMAS spectra were acquired at 19.6 T with a Bruker Avance NEO console, ν_r = 14 kHz MAS, recycle delay of 3.5 s, CT-selective π/2- and π-pulses of 2.5 and 5.0 μs at ν_1 = 50 kHz, and full-echo acquisition with a half-echo delay of 1.0 ms. MQMAS parameters: 3Q hard-pulse (HP) excitation pulse of 20 μs with ν_1 = 110 kHz. All τ_r-pulses were $1/\nu_r$ = 71.43 μs long, single-frequency low-power (lp) pulses were applied with ν_1 = 74.5 kHz at an offset of 588 kHz, while cos τ_r-pulses used ν_1 = 94.3 kHz and an amplitude modulation of 294 kHz, as optimized experimentally. Signal enhancement was applied for all instances of lpMQMAS using a 2 ms WURST-80 pulse with a sweep range equal to ν_r with ν_1 = 25 kHz and a transmitter offset of 588 kHz. The 2D shifted-echo cos-lpMQMAS spectrum was acquired with WURST enhancement, 48 rotor-synchronized t_1 increments, and 96 transients per increment, resulting in a total experiment time of 4.5 h.

4. Conclusions

It has been shown that long τ_r-pulses selective to the satellite-transitions can efficiently interconvert between triple-quantum and central-transition coherences for MQMAS experiments. Using average Hamiltonian theory in the quadrupolar jolting frame, the *rf* spin dynamics of τ_r-pulses can be described by an effective *rf* field for the STs which is scaled by the complex intensity of the spinning sideband irradiated by the *rf* frequency. The anisotropic phase of the spinning sidebands and the effective *rf* field causes signal cancellation for powder samples, which needs to be refocused. One method is to use a pair of identical single-frequency τ_r-pulses as previously reported. In that case, the anisotropic phase from CT → TQ excitation cancels that for TQ → CT conversion. This method requires precise rotor-synchronization between the two τ_r-pulses, otherwise t_1-noise and line broadening appear in the indirect MQ dimension. The second method is to use double-frequency or cosine pulses. The anisotropic phase of the MQ excitation or conversion converges due to the mirror image symmetry of two STs. However, meeting this symmetry condition restricts its bandwidth to less than one spinning frequency, beyond which the phase of the effective *rf* field starts to diverge. The best result is obtained by combining the two methods, i.e., using a pair of cosine τ_r-pulses for MQ excitation and conversion. Both theory and experimental comparisons have shown that the use of two cosine pulses gives an intrinsically higher efficiency than single-frequency τ_r-pulses. Compared to the hard-pulse, FAM and DFS methods, the use of longer cosine τ_r-pulses lowers the required optimal *rf* field to be proportional to $\sqrt{\nu_r \nu_Q}$, facilitating application of cos-lpMQMAS to large C_Qs and/or low-γ quadrupolar nuclei.

Declaration of Competing Interest

The authors declare that they have no known competing financial interests or personal relationships that could have appeared to influence the work reported in this paper.

Acknowledgements

This work was supported by the National High Magnetic Field Laboratory (NHMFL, USA) through NSF DMR-1644779 and the State of Florida.

References

[1] L. Frydman, J.S. Harwood, Isotropic spectra of half-integer quadrupolar spins from bidimensional magic-angle-spinning NMR, J. Am. Chem. Soc. 117 (1995) 5367–5368.
[2] G. Czjzek, J. Fink, F. Gotz, H. Schmidt, J. Coey, J. Rebouillat, A. Lienard, Atomic coordination and the distribution of electric-field gradients in amorphous solids, Phys. Rev. B. 23 (1981) 2513–2530, https://doi.org/10.1103/PhysRevB.23.2513.
[3] D.R. Neuville, L. Cormier, D. Massiot, Al environment in tectosilicate and peraluminous glasses: a 27Al MQ-MAS NMR, Raman, and XANES investigation, Geochim. Cosmochim. Acta. 68 (2004) 5071–5079, https://doi.org/10.1016/j.gca.2004.05.048.
[4] S. Vega, Y. Naor, Triple quantum NMR on spin systems with I = 3/2 in solids, J. Chem. Phys. 75 (1981) 75–86, https://doi.org/10.1063/1.441857.
[5] G. Wu, D. Rovnyak, R.G. Griffin, Quantitative multiple-quantum magic-angle-spinning NMR spectroscopy of quadrupolar nuclei in solids, J. Am. Chem. Soc. 118 (1996) 9326–9332.
[6] A.P.M. Kentgens, R. Verhagen, Advantages of double frequency sweeps in static, MAS and MQMAS NMR of spin I=3/2 nuclei, Chem. Phys. Lett. 300 (1999) 435–443.
[7] P.K. Madhu, A. Goldbourt, L. Frydman, S. Vega, Sensitivity enhancement of the MQMAS NMR experiment by fast amplitude modulation of the pulses, Chem. Phys. Lett. 307 (1999) 41–47.
[8] A. Goldbourt, S. Kababya, S. Vega, P.K. Madhu, The influence of the radiofrequency excitation and conversion pulses on the lineshapes and intensities of the triple-quantum MAS NMR spectra of I = 3/2 nuclei, Solid State Nucl. Magn. Reson. 18 (2000) 1–16, https://doi.org/10.1006/snmr.2000.0007.
[9] A. Goldbourt, P.K. Madhu, S. Vega, Enhanced conversion of triple to single-quantum coherence in the triple-quantum MAS NMR spectrosocopy of spin-5/2 nuclei, Chem. Phys. Lett. 320 (2000) 448–456.
[10] Z. Gan, P.L. Gor'kov, W.W. Brey, P.J. Sideris, C.P. Grey, Enhancing MQMAS of low-gamma nuclei by using a high B-1 field balanced probe circuit, J. Magn. Reson. 200 (2009) 2–5.
[11] H. Colaux, D.M. Dawson, S.E. Ashbrook, Efficient amplitude-modulated pulses for triple- to single-quantum coherence conversion in MQMAS NMR, J. Phys. Chem. A. 118 (2014) 6018–6025, https://doi.org/10.1021/jp505752c.
[12] I. Hung, Isotropic solid-state MQMAS NMR spectra for large quadrupolar interactions using satellite-transition selective inversion pulses and low rf fields, J. Magn. Reson. 324 (2021), https://doi.org/10.1016/j.jmr.2021.106913 106913.
[13] I. Hung, Z. Gan, Low-power STMAS – breaking through the limit of large quadrupolar interactions in high-resolution solid-state NMR spectroscopy, Phys. Chem. Chem. Phys. 22 (2020) 21119–21123, https://doi.org/10.1039/d0cp04274a.
[14] I. Hung, P. Gor'kov, Z. Gan, Efficient and sideband-free 1H-detected 14N magic-angle spinning NMR, J. Chem. Phys. 151 (2019) 154202, https://doi.org/10.1063/1.5126599.
[15] P. Caravatti, G. Bodenhausen, R.R. Ernst, Selective pulse experiments in high-resolution solid state NMR, J. Magn. Reson. 55 (1983) 88–103, https://doi.org/10.1016/0022-2364(83)90279-2.
[16] A.J. Pell, K.J. Sanders, S. Wegner, G. Pintacuda, C.P. Grey, Low-power broadband solid-state MAS NMR of 14N, J. Chem. Phys. 146 (2017) 194202.
[17] M. Bak, J.T. Rasmussen, N.C. Nielsen, SIMPSON: A general simulation program for solid-state NMR spectroscopy, J. Magn. Reson. 147 (2000) 296–330.
[18] J.J. Sakurai, Modern Quantum Mechanics, Rev. Ed., Addison-Wesley Publishing Company Inc, Reading, Massachusetts, 1994.
[19] P.K. Madhu, A. Goldbourt, L. Frydman, S. Vega, Fast radio-frequency amplitude modulation in multiple-quantum magic-angle-spinning nuclear magnetic resonance: theory and experiments, J. Chem. Phys. 112 (2000) 2377–2391, https://doi.org/10.1063/1.480804.
[20] J. Skibsted, H.J. Jakobsen, Variable-temperature Rb-87 magic-angle spinning NMR spectroscopy of inorganic rubidium salts, J. Phys. Chem. A. 103 (1999) 7958–7971.
[21] D. Massiot, B. Touzo, D. Trumeau, J.P. Coutures, J. Virlet, P. Florian, P.J. Grandinetti, Two-dimensional magic-angle spinning isotropic reconstruction sequences for quadrupolar nuclei, Solid State Nucl. Magn. Reson. 6 (1996) 73–83.
[22] Z.H. Gan, H.T. Kwak, Enhancing MQMAS sensitivity using signals from multiple coherence transfer pathways, J. Magn. Reson. 168 (2004) 346–351.
[23] J.-P. Amoureux, C. Fernandez, L. Frydman, Optimized multiple-quantum magic-angle spinning NMR experiments on half-integer quadrupoles, Chem. Phys. Lett. 259 (1996) 347–355, https://doi.org/10.1016/0009-2614(96)00809-3.
[24] I. Hung, J. Trebosc, G.L. Hoatson, R.L. Vold, J.P. Amoureux, Z. Gan, Q-shear transformation for MQMAS and STMAS NMR spectra, J. Magn. Reson. 201 (2009) 81–86.
[25] T. Vosegaard, I.P. Byriel, L. Binet, D. Massiot, H.J. Jakobsen, Crystal structure studies by single-crystal NMR spectroscopy. Ga-71 and Ga-69 single-crystal NMR of beta-Ga2O3 twins, J. Am. Chem. Soc. 120 (1998) 8184–8188.